

Observations and numerical simulations of the diurnal cycle of the EUROCS stratocumulus case

Peter G. Duynkerke^{1*}, Stephan R. de Roode^{1 †}, Margreet C. van Zanten¹, Javier Calvo²,
Joan Cuxart², Sylvain Cheinet³, Andreas Chlond⁴, Hervé Grenier⁵, Piet J. Jonker¹,
Martin Köhler⁶, Geert Lenderink⁷, David Lewellen⁸,
Cara-Lyn Lappen⁹, Adrian P. Lock¹⁰, Chin-Hoh Moeng¹¹,
Frank Müller⁴, Dolores Olmeda², Jean-Marcel Piriou⁵,
Enrique Sanchez², Igor Sednev⁴

¹ Institute for Marine and Atmospheric Research Utrecht, The Netherlands

² Instituto Nacional Meteorologia, Madrid, Spain

³ Laboratoire de Météorologie Dynamique, Paris, France

⁴ Max-Planck Institut für Meteorologie, Hamburg, Germany

⁵ Meteo France, Toulouse, France

⁶ European Centre for Medium-Range Weather Forecasts, Reading, United Kingdom

⁷ Royal Netherlands Meteorological Institute, De Bilt, The Netherlands

⁸ West Virginia University, Morgantown, West Virginia, USA

⁹ Colorado State University, Fort Collins, Colorado, USA

¹⁰ Met Office, Bracknell, Berkshire, United Kingdom

¹¹ National Center for Atmospheric Research, Boulder, Colorado, USA

Revised version submitted to the Quart. J. R. Met. Soc. EUROCS special
issue, March 24, 2004

*Deceased 19 January 2002

†Corresponding author address: Stephan R. de Roode, Institute for Marine and Atmospheric Research Utrecht (IMAU), Princetonplein 5, 3584 CC Utrecht, The Netherlands.
Phone: +31 30 2532909. Email: roode@phys.uu.nl

Abstract

As part of the European Project on Cloud Systems in Climate Models (EUROCS) the diurnal cycle of stratocumulus has been simulated with Large-Eddy Simulation (LES) models and Single Column Models (SCMs). The models were initialized and compared with observations collected in marine stratocumulus in July 1987 during the First ISCCP (International Satellite Cloud Climatology Project) Regional Experiment (FIRE). The results of the six LES models are found to be in a fair agreement with the observations. They all capture the distinct diurnal variation in the cloud liquid-water path, the turbulence profiles and clearly show a decoupled boundary layer during daytime and a vertically well-mixed boundary layer during the night. Entrainment of relatively dry and warm air from just above the inversion into the boundary layer is the major process modifying the thermodynamic structure of the boundary layer during the night. The differences that arise in the liquid-water path evolution can therefore be attributed mainly to differences in the entrainment rate. The mean entrainment rates computed from the LES model results are $0.58 \pm 0.08 \text{ cm s}^{-1}$ and $0.36 \pm 0.03 \text{ cm s}^{-1}$ for the night-time and daytime periods, respectively. If the horizontal domain size in a LES model is enlarged, mesoscale fluctuations develop. This leads to a broader liquid-water path distribution and a reduction of the cloud albedo.

To assess the quality of the representation of stratocumulus in General Circulation Models, results from ten SCMs are compared with observations and LES results. The SCM latent and sensible heat fluxes at the surface agree fairly well with the LES results. Many of the SCMs predict a much too low liquid-water path, a cloud cover smaller than unity, and cloud tops that are lower than the observations and the LES results. This results in a much larger amount of downwelling short-wave radiation absorbed at the sea surface. Improvement of entrainment parametrizations is needed for a better representation of stratocumulus in SCMs.

Observations and LES results of entrainment rates for different stratocumulus cases are compared. The observed entrainment rates in Atlantic stratocumulus clouds during ASTEX are larger than for the ones over the Pacific Ocean off the coast of California. Results from LES models corroborate these findings. The differences in the entrainment rate can likely be attributed to the smaller inversion jumps of the liquid water potential temperature for the ASTEX stratocumulus cases.

1. Introduction

The presence of a stable temperature inversion at the top of the atmospheric boundary layer, and the availability of sufficient moisture are the major ingredients for the formation and maintenance of stratocumulus clouds. For these reasons, extended marine stratocumulus-topped boundary layers (STBLs) are often found above the subtropical oceans in the descending branches of the Hadley circulation (Klein and Hartmann, 1993; Norris, 1997a,b). Figure 1 shows a striking example of a solid stratocumulus deck above the Pacific Ocean off the coast of California, and clear skies over the continent. Due to its high albedo, stratocumulus clouds strongly diminish the solar insolation of the Earth's surface during daytime. On the other hand, stratocumulus clouds are often sufficiently optically thick such that long-wave radiation is emitted as a black body just like the underlying ocean surface. These radiative properties make stratocumulus an important factor in determining the Earth's surface energy balance.

In atmospheric General Circulation Models (GCMs), however, the amount of subtropical marine stratocumulus is usually underpredicted, even when the observed Sea Surface Temperatures (SSTs) are prescribed (Jakob, 1999). Duynkerke and Teixeira (2001) compared ECMWF Re-Analysis (ERA) results with observations from the First ISCCP (International Satellite Cloud Climatology Project) Regional Experiment (FIRE) experiment (Albrecht et al., 1988). Their study showed that the ERA cloud cover and liquid-water path (LWP) are strongly underestimated, which causes the ERA downwelling short-wave radiation at the surface to be much larger than observed. Ma et al. (1996) demonstrate that in a coupled atmosphere-ocean model an underestimation of the stratocumulus cloud amount can lead to positive SST biases of about $5K$. This is of a particular concern for simulations and predictions of El Niño - Southern Oscillation (ENSO), since such errors can strongly affect the (sub) tropical circulations (Philander et al., 1996; Nigam, 1997; Yu and Mechoso, 1999). Furthermore, the presence of subtropical stratocumulus fields plays an important role in the entire tropical response to climate perturbations (Miller, 1997). It is therefore vitally important that in GCMs stratocumulus cloud fields are accurately represented.

Stratocumulus clouds can exhibit a marked diurnal cycle (Wood et al., 2002). During the night turbulence is driven by a strong long-wave radiative cooling near the top of the stratocumulus cloud. This usually results in vertically well-mixed STBLs. In contrast, the STBL can become decoupled during daytime due to absorption of solar radiation in the cloud layer. This implies that the cloud layer becomes stably stratified with respect to the sub-cloud layer, and the transport of heat and moisture from the surface into the cloud layer will be effectively reduced or will even be cut off. Because entrainment maintains a steady supply of relatively warm and dry air from above the inversion into the cloud layer, the cloud layer can rapidly thin or even disappear during daytime.

The EUROpean Cloud Systems (EUROCS) project used observations made in stratocumulus off the coast of California during FIRE I (Hignett, 1991; Duynkerke

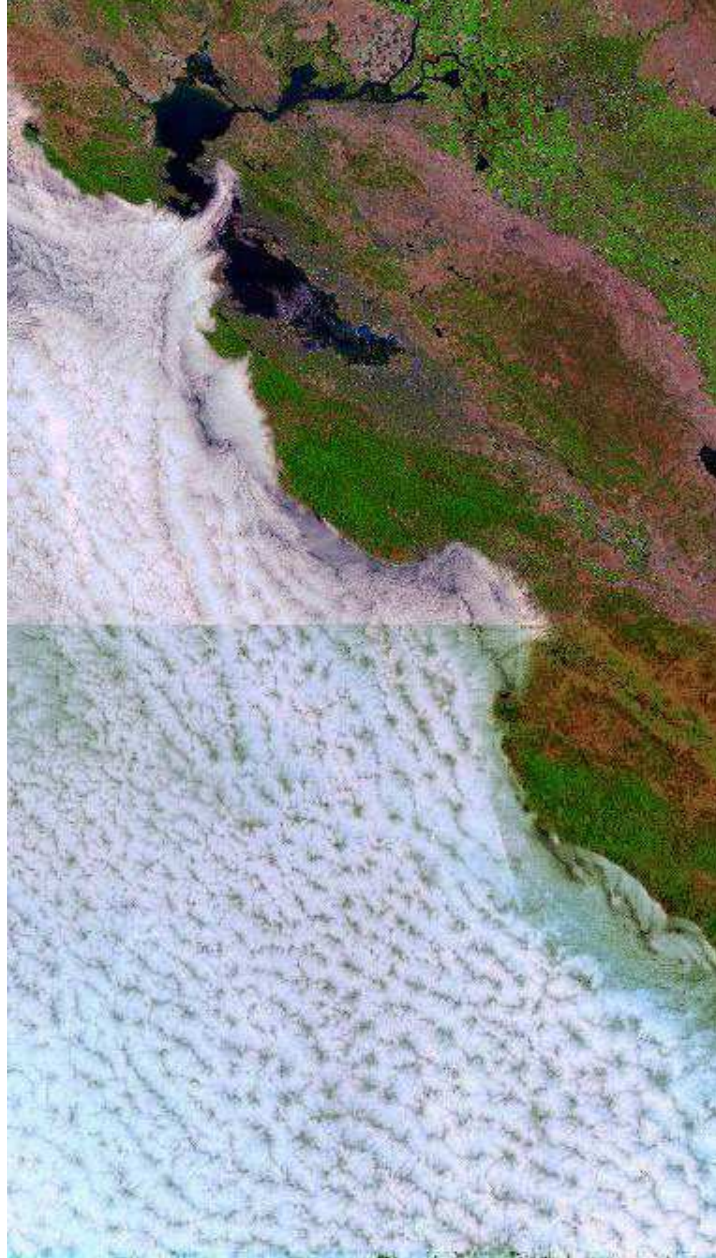


Figure 1: Landsat satellite image (horizontal area about $200 \times 400 km^2$) showing stratocumulus off the coast of California for 14 July 1987. The cloud tops are at about $500 \sim 1000 m$ whereas the convective cells have a horizontal dimension of about $10 km$. The stratocumulus case studied in this paper is based on observations performed during FIRE I in the cloud deck shown.

and Hignett, 1993) as a basis to set up a well-defined case for modeling the diurnal cycle of stratocumulus. The modeling results can be verified with observations of cloud cover, liquid-water path, cloud-base and cloud-top height, downwelling and short-wave radiation at the surface, and the turbulence structure of the boundary layer. The EUROCS stratocumulus diurnal cycle case adds to previous intercomparison studies that addressed other boundary-layer cloud regimes such as nocturnal stratocumulus (Moeng et al., 1996; Duynkerke et al., 1999), a stratocumulus to cumulus transition over the Atlantic Ocean observed during ASTEX (Bretherton et al., 1999), trade-wind cumuli capped by a strong inversion in ATEX (Stevens et al., 2001), the diurnal cycle of shallow cumulus convection over land from ARM (Brown et al., 2002) and shallow cumulus over the ocean based on observations collected during BOMEX (Siebesma et al., 2003). This study is a piece in the EUROCS chain that links detailed studies on a particular cloud regime like stratocumulus, cumulus (Lenderink et al., 2003) and deep convection (Guichard et al., 2004), to the representation of these cloud types in the Hadley circulation (Siebesma et al., 2004).

A detailed description of the EUROCS stratocumulus case is given in Section 2. Section 3 discusses LES results of the surface energy balance, the turbulence structure of the STBL, and the development of mesoscale fluctuations. The representation of stratocumulus in ten GCMs for weather and climate and Regional Climate Models is assessed from a comparison of the surface energy balance obtained with their respective Single Column Model (SCM) versions. Because the development of parametrizations for the entrainment rate in the STBL is currently one of the most challenging problems in boundary-layer meteorology, observations and LES results of entrainment rates for different stratocumulus cases are compared in Section 4. Various suggestions for model improvements are summarized in Section 5, and Section 6 presents the main findings.

2. Observations and model initialization of the EUROCS stratocumulus case

a. Surface based observations

The FIRE I stratocumulus experiment performed off the coast of southern California in July 1987 provides a very comprehensive set of data on marine stratocumulus from airborne, ground-based and satellite instruments (Albrecht et al., 1988). Several instruments were installed on San Nicolas island, approximately $33^{\circ}15'N$ and $119^{\circ}30'W$, to monitor cloud properties with a high temporal resolution. Cloud-base height was measured by a Väisälä CT 12K laser ceilometer (Schubert et al., 1987). A sodar was used to estimate the inversion height (White, 1999). The vertically integrated liquid water content was retrieved using a three-channel (20.6, 21.65 and 90.0 GHz) microwave radiometer as described by Hogg et al. (1983). The temporal evolution of the cloud conditions on San Nicolas Is-

land during July 1987 is discussed in detail by Blaskovic et al. (1991), Betts (1990) and Albrecht et al. (1990). In addition, Hignett (1991) and Duynkerke and Hignett (1993) present the turbulence structure in the boundary layer as measured on 14 and 15 July 1987 by means of an instrumented tethered balloon.

b. Initial and boundary conditions

During 1 to 19 July 1987 sixty-nine vertical profiles of the temperature and the relative humidity were measured by radiosondes. From these data mean vertical profiles for the potential temperature and specific humidity were calculated by Duynkerke and Teixeira (2001), which are shown in Figure 2. Because the inversion height is quite variable in time the inversion structure is smeared out in the averaged profile. To quantify the strength of the inversion the jumps in liquid water potential temperature and total water content were estimated from each individual sounding as well. This was done in a method similar to Kuo and Schubert (1988). For each of the soundings we determined the cloud-top jump in total water Δq_t as follows. First the height of the inversion base was determined from the level above which the potential temperature strongly increases with height. Next, we computed the vertically averaged specific humidity in the layer 200 m above the inversion. Finally, we subtracted from this the average specific humidity in the layer which extends from 65 to 165 m above sea level (the island sounding site being 38 m above sea level). If the boundary layer is vertically well mixed the specific humidity difference should be equivalent to the jump in total water at cloud top. The procedure for $\Delta \theta_l$ is identically done with θ . In this way each sounding is characterized by a point in the $(\Delta \theta_l, \Delta q_t)$ plane as shown in Figure 3. The average jump at cloud top is given by $\Delta \theta_l = 12 \text{ K}$ and $\Delta q_t = -3.0 \text{ g kg}^{-1}$.

Figure 2 also shows the initial vertical profiles for liquid water potential temperature (θ_l) and total water content (q_t),

$$\begin{aligned} 0 < z \leq 595 \text{ m} & \begin{cases} \theta_l = 287.5 \text{ K} \\ q_t = 9.6 \text{ g kg}^{-1} \end{cases} \\ 595 < z \leq 1200 \text{ m} & \begin{cases} \theta_l = 299.5 + 0.0075(z - 595) \text{ K} \\ q_t = 6.6 - 0.003(z - 595) \text{ g kg}^{-1} \end{cases} \end{aligned} \quad (1)$$

A comparison of the monthly mean values with observed vertical profiles during 14 and 15 July indicates that in the free atmosphere the total water contents are nearly the same, but the monthly mean potential temperature is about 5 K colder. The initial total water content in the boundary layer is set to a value that is close to the observations during 14 and 15 July, in order to give an initial cloud-base height of about 250m.

The large-scale surface pressure gradient for July 1987 (Figure 2 of Duynkerke and Teixeira (2001)) gives a geostrophic wind direction (counter-clockwise with respect to the x -direction) of about $\alpha_g = 305^\circ$. Due to the surface friction the observed boundary layer wind direction α deviates from the geostrophic value. This

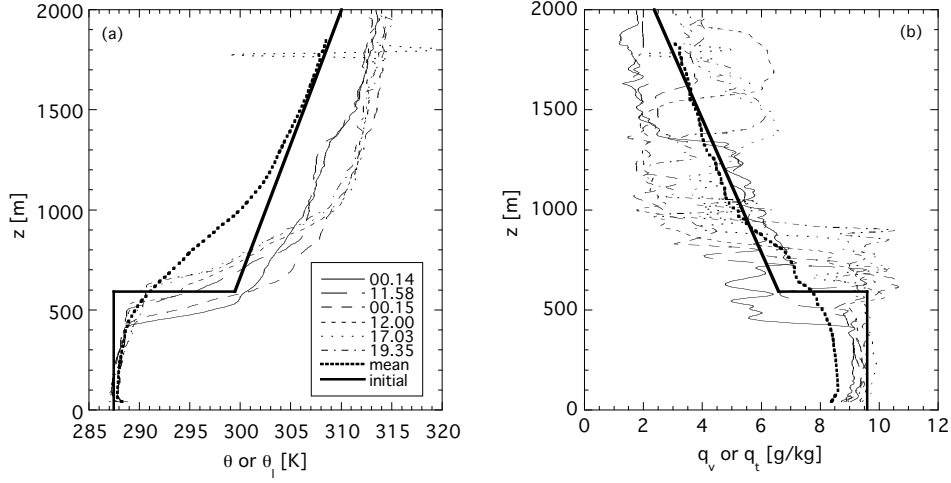


Figure 2: The observed vertical profiles of the a) potential temperature θ and the b) specific humidity q_v at 0014 and 1158 UTC 14 July and 0015, 1200, 1703 and 1935 UTC 15 July. The mean of the observed profiles collected between 1 and 19 July 1987 is indicated by the thick dashed line. The thick solid lines are the initial conditions for the liquid water potential temperature (θ_l) and total water content (q_t) prescribed in the models. The linestyles are according to the legend displayed in the left panel.

value for α was observed on 14 and 15 July 1987 at San Nicolas island by Hignett (1991) as well. The geostrophic wind speed is prescribed as $U_g = 6.0 \text{ m s}^{-1}$, and the resulting geostrophic forcing in the (x, y) direction is thus: $(u_g, v_g) = U_g(\cos \alpha_g, \sin \alpha_g)$. In the models the initial wind fields were set to the geostrophic winds

$$(u, v) = U_g(\cos \alpha_g, \sin \alpha_g). \quad (2)$$

The surface temperature and pressure are prescribed as $T_s = 289.0 \text{ K}$ and $p_s = 1012.5 \text{ hPa}$, respectively (Duynderke and Teixeira, 2001). Because the wind is blowing almost parallel to the isotherms of the sea surface temperature this means that the surface temperature hardly changes as the air flows south-eastwards (Duynderke and Hignett, 1993). The specific humidity at the sea-surface is set to its saturated value at the sea-surface temperature, $q_s = 11.1 \text{ g kg}^{-1}$. The surface roughness length is set to $2 \times 10^{-4} \text{ m}$, and the Coriolis parameter $f = 8.0 \times 10^{-5} \text{ s}^{-1}$ (33.3° N , 119.5° W).

c. Forcings

The large-scale subsidence rate \bar{w} is prescribed as,

$$0 < z \leq 1200 \text{ m} \quad \bar{w} = -1 \times 10^{-5} z \text{ m s}^{-1}. \quad (3)$$

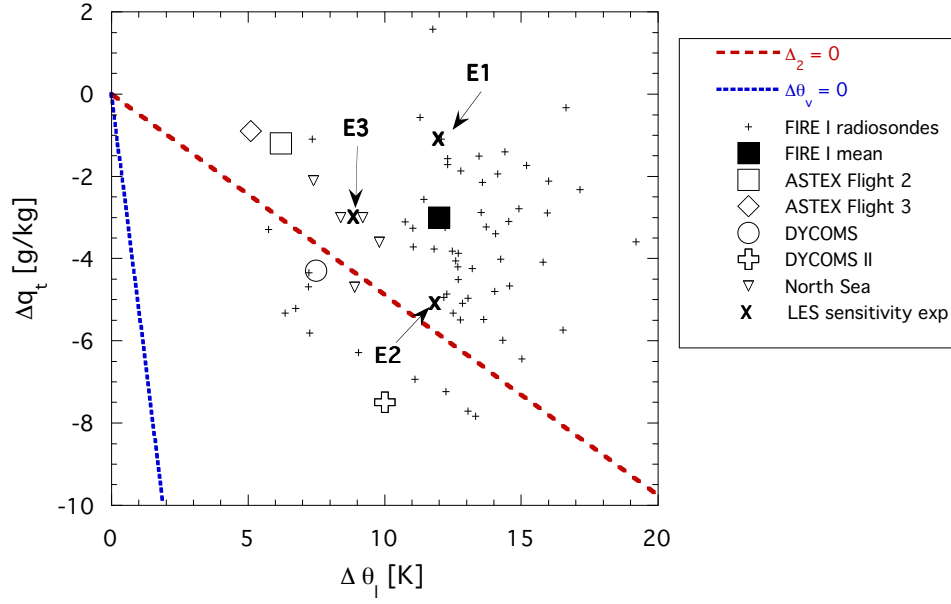


Figure 3: The $(\Delta\theta_l, \Delta q_t)$ plane. It shows the thermodynamic instability curve for the clear convective boundary layer $\Delta\theta_v = 0$ and the cloud-top instability criterion proposed by Randall (1980) and Deardorff (1980), $\Delta_2 = 0$. Plotted are sixty-two points obtained from high vertical resolution soundings taken from 30 June to 19 July 1987 on San Nicolas island. Also shown are the mean inversion jumps of stratocumulus cases observed during Flights 2 and 3 of the ASTEX First Lagrangian (De Roode and Duynkerke, 1997), DYCOMS (Kawa and Pearson Jr, 1989), Flight RF01 of DYCOMS II (Stevens et al., 2003) and five flights performed over the North Sea (Nicholls and Leighton, 1986). The jumps of three LES sensitivity experiments have been indicated by arrows. The line styles and symbols are according to the legend.

It is hard to obtain the large-scale subsidence rate directly from observations. The subsidence rate in Eq. (3) is based on test simulations with the IMAU LES model, and approximately balances the diurnally-averaged entrainment rate. Eq. (3) gives subsidence rates that are nearly a factor of two larger than the average values over San Nicholas Island presented by Neiburger (1960).

To balance the subsidence heating and drying above the boundary layer a large-scale (LS) advection term is included in the simulation:

$$0 < z \leq 1200 \text{ m} \begin{cases} \left(\frac{d\theta_t}{dt} \right)_{LS} = -7.5 \times 10^{-8} \max(z, 500) & (K s^{-1}) \\ \left(\frac{dq_t}{dt} \right)_{LS} = 3.0 \times 10^{-11} \max(z, 500) & (kg \text{ kg}^{-1} s^{-1}). \end{cases} \quad (4)$$

In the boundary layer the large-scale horizontal advection tendencies approximately counteract the divergence of the turbulent fluxes of heat and moisture. The u, v, θ_l and q_t profiles in the damping layer are relaxed towards the geostrophic wind and initial thermodynamic profiles (1) and (2), respectively.

The net upward long-wave radiation is parametrized as:

$$F_l(z) = \Delta F_t e^{-a \text{LWP}(z, z_t)}, \quad (5)$$

where $\Delta F_t = 70 W m^{-2}$ (Duda et al., 1991) is the long-wave radiative flux divergence at the cloud top, $a = 130 m^2 kg^{-1}$ a constant, $z_t = 1200 m$ the top of the model domain. The liquid-water path between z_1 and z_2 is given by

$$\text{LWP}(z_1, z_2) = \int_{z_1}^{z_2} \rho_0 q_l dz, \quad (6)$$

where $\rho_0 = 1.14 kg m^{-3}$ is the mean density and q_l is the liquid water content.

The solar radiation is a function of the solar zenith angle θ_0 ($\mu_0 = \cos \theta_0$) and the optical depth τ which is parametrized as:

$$\tau(z) = \frac{3 \text{LWP}(z, z_t)}{2 r_e \rho_l} \quad (7)$$

where $r_e = 10 \mu m$ is the effective radius and $\rho_l = 1000 kg m^{-3}$ is the density of water. The net downward short-wave radiation F_s is obtained from the analytical solution of the delta-Eddington approximation, which is summarized in the Appendix. The removal of liquid water by precipitation was not taken into account.

d. Models

In total six LES models and ten SCMs have participated in this study (see Table 1). Details about the numerical codes of these LES models can be found in Duynkerke et al. (1999), Stevens et al. (2001), Brown et al. (2002), and Siebesma et al. (2003). Periodic lateral boundary conditions were applied to the LES models. A spatially uncorrelated random perturbation between -0.1 and 0.1 K was applied to the initial

Participating scientists	Institution	LES	SCM	$N_{BL,SCM}$
M. C. van Zanten	IMAU	Y		
A. Chlond, I. Sednev, F. Müller	MPI	Y	ECHAM	9
A. P. Lock	UKMO	Y	UKMO	6
E. Sanchez, D. Olmeda, J. Calvo	INM		HIRLAM	8
E. Sanchez, J. Cuxart	INM	Y	MESO-NH	60
C.-H. Moeng	NCAR	Y		
D. Lewellen	WVU	Y		
G. Lenderink	KNMI		RACMO	59
C.-L. Lappen	CSU		Mass-flux	60
S. Cheinet	LMD		LMD GCM	12
H. Grenier	MetFr I		ARPEGE Climate	3
J. M. Piriou	MetFr II		ARPEGE NWP	6
M. Köhler	ECMWF		ECMWF	8

Table 1: Participating Large-Eddy Simulation and Single-Column models. The acronyms represent the name of the participating scientists’ institution. $N_{BL,SCM}$ indicates the number of vertical grid points in the boundary layer ($0 < z \leq 595\text{ m}$) after initialization at $t = 0000h$ LT for the respective SCMs.

temperature field at all grid points. Throughout the domain an initial value for sub-grid TKE of $1\text{ m}^2\text{s}^{-2}$ was specified. The grid size in the horizontal is 50 m and in the vertical 10 m , covering a domain of 2.5 km in x and y and 1.2 km in z .

Ten Single-Column Model versions of (semi-)operational numerical weather prediction and climate models were used. In a SCM the large-scale tendencies are prescribed, while the non-advective tendencies of prognostic variables are predicted by the model’s physical parametrizations. Details of the ARPEGE, ECMWF, ECHAM, RACMO, UKMO, MESO-NH and HIRLAM boundary-layer mixing schemes are summarized by Lenderink et al. (2003), who report on the EUROCS SCM intercomparison of the diurnal cycle of shallow cumulus over land. The CSU-SCM model is an unified mass-flux model that has been developed recently by Lappen and Randall (2001). It includes a prognostic equation for the vertical mass-flux, and vertical fluxes are proportional to the vertical massflux and the difference between the updraft and downdraft value of the quantity. The mixing scheme of the single-column version of the LMD GCM utilizes a K-profile approach (Cheinet, 2002). Note that because most of the SCMs are the operational versions of their parent GCMs, the radiation codes suggested in this paper were not implemented in all SCMs, and the models may generate precipitation or shallow cumulus convection by their microphysics and convection schemes, respectively. Additional sensitivity experiments have been carried out to assess the role of the vertical resolution and the convection scheme.

Because in the EUROCS stratocumulus case the radiation and large-scale forcings are prescribed, variations in the tendencies of heat and moisture must be pri-

marily attributed to the SCM’s turbulent transport and cloud schemes. As such possible deficiencies in the boundary-layer parameterization package are straightforwardly to identify.

Since the initial state is reasonably close to the radiosonde soundings during 14 and 15 July, we will compare the model results with observations from this period. The model simulations start at 14 July 0800 UTC (= 0000 *h* Local Time (LT)) and last at least 37 hours. Since the monthly-mean atmospheric state does not differ very much from the initial profiles either, we will present monthly-mean values of the observations, too.

3. Simulation results

a. Surface energy balance

i. Large-Eddy Simulation results The surface energy balance reads,

$$-G = H + LE + F_s + F_l, \quad (8)$$

where H and LE represent the surface sensible and latent heat fluxes, respectively, and F_s and F_l the net short-wave and long-wave radiative fluxes, respectively. The net energy flow into the ocean, $-G$, is computed as a residual. According to Table 2, the computed turbulent fluxes of heat and moisture at the surface are rather consistent among the LES models, and the net short-wave radiative flux is the dominant component of the surface energy balance. Because the cloud droplet effective radius used in the LESs has a constant value, the transmissivity of the cloud layer depends only on the LWP, as can be seen from Eq. (7). Therefore, the differences in the net short-wave radiative fluxes are entirely due to the variations in the computed LWPs. Inspection of the mean LWP values shows that larger numbers for the LWP correspond to smaller numbers of the net short-wave radiative flux, and vice versa. The values for the diurnal mean LWP from the LES models range from a minimum of 93 (IMAU) to a maximum of 168 gm^{-2} (UKMO).

In Figure 4 the LWPs from the LES models are compared with the retrievals of the microwave radiometer from 14 and 15 July 1987, and the hourly monthly-mean diurnal variation. All the LESs capture the strong diurnal variation in LWP due to the forcing imposed by the short-wave heating on the cloud layer. Like the observations, the maximum cloud thickness is found during the night, and the cloud deck gradually thins until noon. However, the thinning is not sufficient to break up the cloud; in all the LESs the cloud cover remains equal to unity. After 30 hours of simulation time the difference between the minimum (IMAU) and maximum (UKMO) values for the modeled LWP ranges by nearly a factor of two. This variation is about as large as the difference between the monthly mean and observed diurnal cycle. Note that the LWP is very sensitive to small changes in the thermodynamic structure of the boundary layer. If the boundary layer is vertically well-mixed then the liquid water content q_l increases approximately linearly with

Model	H [Wm^{-2}]	LE [Wm^{-2}]	F_s [Wm^{-2}]	F_l [Wm^{-2}]	G [Wm^{-2}]	LWP [gm^{-2}]
IMAU	4.0	27.3	-196	0.1	165	93
MPI	4.1	23.0	-171	0.0	144	116
UKMO	7.5	20.4	-124	0.0	96	168
INM	5.1	22.6	-164	0.0	136	130
NCAR	13.9	24.3	-190	0.0	152	110
WVU	8.6	28.1	-185	0.0	148	95
LES MEAN	7.2 ± 3.8	24.3 ± 2.9	-172 ± 26	0.02 ± 0.04	140 ± 24	119 ± 28
Observations			-114			130
Monthly mean observations			-185			73

Table 2: LES results of the mean surface energy balance from 1200 to 3600 h LT. The columns show the sensible heat flux H , the latent heat flux LE , the net short-wave radiative flux F_s , the net long-wave radiative flux F_l and the energy flow into the sea surface G . The last column shows the mean liquid water path. The observed mean values are computed from measurements collected on 14 and 15 July 1987 from 0000 to 4800 h LT, and the monthly mean values represent averages from data collected between 1 and 19 July 1987. Note that we computed the net short-wave radiation from the observed downwelling component assuming a ground albedo $A_g = 0.05$.

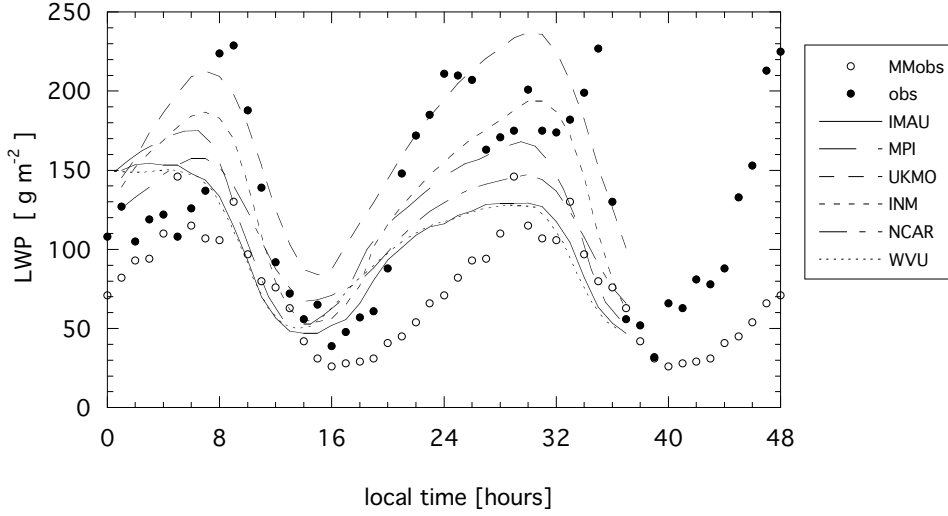


Figure 4: The observed and modeled LWP from six different LES models as a function of time for 14 and 15 July 1987 (denoted from 0 to 48 hours Local Time). The filled dots are the hourly mean observed values (obs) whereas the open circles are the hourly monthly-mean values (MMobs). The linestyles (LES results) are according to the legend.

height. In that case, from (6) it follows that (Albrecht et al., 1990)

$$LWP \propto (c_t - c_b)^2, \quad (9)$$

where c_t and c_b represent the cloud-top and cloud-base heights. As an example, for the EUROCS stratocumulus case this implies that for a cloud layer that is 350 m thick, a change of just 20 m leads to a subsequent variation in the LWP of nearly 12%.

Figure 5 compares the modeled cloud-base and cloud-top height evolution to the observations. The top of a stratocumulus cloud layer is usually located just below the inversion height z_i , the latter of which varies with time according to

$$\frac{dz_i}{dt} = \overline{w}(z_i) + w_e. \quad (10)$$

An inspection of the cloud-top height evolution therefore gives a good appreciation of differences in the entrainment rate. After 37 hours simulation time the typical scatter in the cloud-top heights is about 100 m. Such a variation corresponds roughly with a typical difference in the mean entrainment rate on the order of 1 mm s^{-1} . The differences in the cloud layer depth are mainly due to variations in the simulated cloud-base height. The lowest cloud bases are due to larger moistening rates of the boundary layer, and are found for models that simulate the smallest entrainment rates. There is a much larger amplitude in the observed cloud-top height during the first diurnal cycle than in the simulations. Possibly, a diurnal

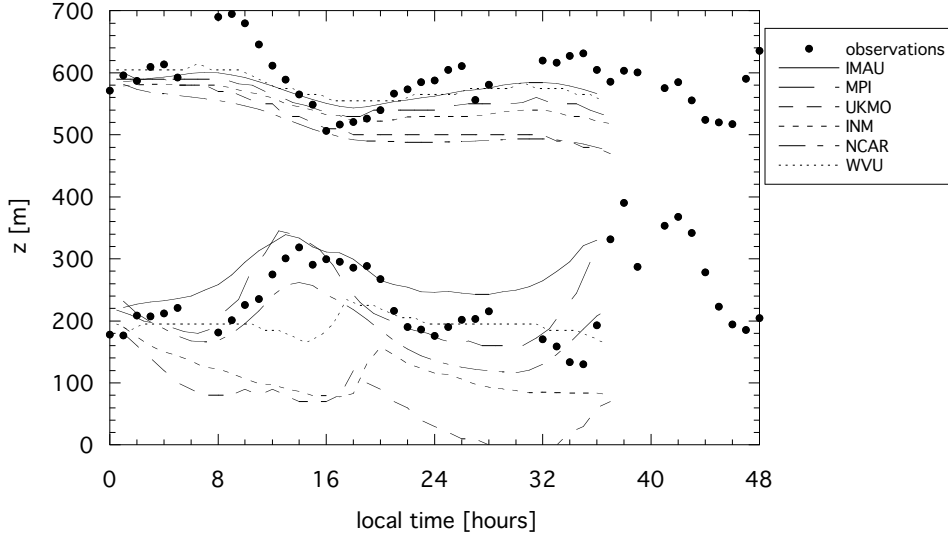


Figure 5: The cloud-base and cloud-top height from observations and Large-Eddy Simulations as a function of time for 14 and 15 July 1987 (denoted from 0 to 48 hours Local Time). The linestyles are according to the legend.

cycle in the subsidence rate may play a role, as was found from an observational study of stratocumulus over the southeast Pacific region (Bretherton et al., 2004).

ii. *Single-Column Model results* Table 3 displays the mean surface energy balance components as computed by the SCMs. The turbulent fluxes at the surface compare well with the LES model results. The scatter in the liquid-water paths, shown in Figure 6, is reflected in the amount of downwelling short-wave radiation absorbed at the sea surface, which varies considerably among the SCMs. About half of the SCMs compute lower values for the LWP than is observed. These models give a much larger amount of downwelling short-wave radiation absorbed at the sea surface. This error may be partly counteracted by a significant decrease in the downwelling long-wave radiation at the sea surface due to a decrease of the cloud emissivity.

Figure 7 shows that the majority of the SCMs tend to compute a cloud-top height that is too low in comparison to the observations and LES results. According to Eq. (10) this suggests that for these SCMs the entrainment rate is probably too low. In contrast to the observations, some SCMs compute a cloud cover less than unity, in particular during daytime (see Figure 8). Because the latent and sensible heat fluxes at the surface in the SCMs and the LESs are in a fairly good agreement, any different entrainment rate of heat and moisture will probably explain a good deal of the discrepancy in the simulated cloud evolution. A better representation of stratocumulus clouds in GCMs can likely be achieved by improving the parametrization of entrainment. In the next section this topic will be discussed in

Model	H [Wm^{-2}]	LE [Wm^{-2}]	F_s [Wm^{-2}]	F_l [Wm^{-2}]	G [Wm^{-2}]	LWP [gm^{-2}]
KNMI RACMO	4.0	26.2	-272	10.3	232	33
INM MESO-NH	6.2	21.0	-130	0.0	103	159
INM HIRLAM	6.7	17.4	-191	0.0	167	98
CSU Mass-flux	14.8	24.5	-119	0.0	80	161
LMD GCM	0.2	15.9	-237	20.8	200	41
MPI ECHAM	5.5	29.6	-119	8.2	76	156
MetFr ARPEGE Climate	24.0	24.0	-262	0.3	214	57
UKMO	10.3	26.0	-173	15.7	121	75
MetFr ARPEGE NWP	4.3	17.9	-306	78.4	205	14
ECMWF	5.3	21.4	-249	21.8	200	87
SCM MEAN	8.1 ± 6.8	22.4 ± 4.4	-206 ± 69	15.6 ± 23.7	160 ± 59	88 ± 55

Table 3: SCM results of the mean surface energy balance from 1200 to 3600 h LT. The columns show the sensible heat flux H , the latent heat flux LE , the net short-wave radiative flux F_s , the net long-wave radiative flux F_l and the energy flow into the sea surface G . The last column shows the mean liquid water path.

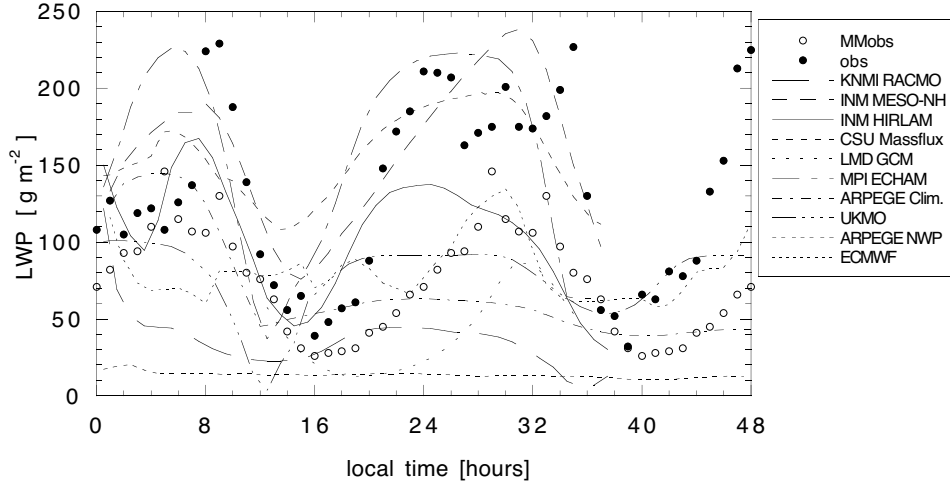


Figure 6: The observed and modeled LWP from ten different SCM models as a function of time for 14 and 15 July 1987 (denoted from 0 to 48 hours Local Time). The filled dots are the hourly mean observed values (obs) whereas the open circles are the hourly monthly-mean values (MMObs). The linestyles are according to the legend.

detail.

Clearly, there is wide disagreement in the SCM results. Some models predict a cloud layer that gradually dissipates, whereas other models maintain a solid cloud layer. The analysis of the model results is complicated by the different physical packages that have been used. Therefore, a few additional sensitivity experiments were carried out to explore the role of the microphysics scheme, the convection scheme, and the effect of the vertical resolution. In the Conv_Off (Conv_On) simulations the convection routine was turned off (on). In the Conv_off run the turbulence mixing scheme is taking care of all turbulent transports in the cloud layer. In the ECHAM and RACMO models the turbulence scheme is based on moist physics, which enables the simulation of realistic transports of heat and moisture in the cloud layer. These simulations exclude precipitation, and the long-wave and short-wave radiation routines were coded according to the case set-up. This approach facilitates a direct comparison with the LES results, and these two simulations are intended to verify the performance of the PBL models at representing stratocumulus convection excluding all other model components but vertical advection. As the PBL gets decoupled during the day, it is relevant to evaluate also cumulus convection schemes in this context. These SCM simulations were done on a vertical resolution as is currently implemented in the ECMWF model (60 levels vertical resolution, with 8 grid levels in the boundary layer at the initialization time). To assess the role of the vertical grid resolution and to minimize the effect of numerical errors two additional experiments were done on a finer vertical resolution (12 grid levels in the boundary layer), labeled as Conv_Off_HR and

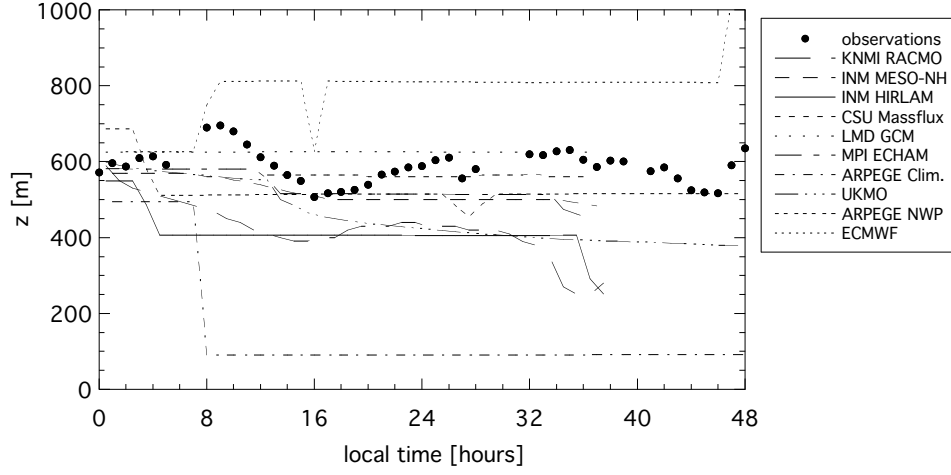


Figure 7: The cloud-top height from observations (filled dots) and Single-Column Model simulations as a function of time for 14 and 15 July 1987 (denoted from 0 to 48 hours Local Time). The linestyles are according to the legend.

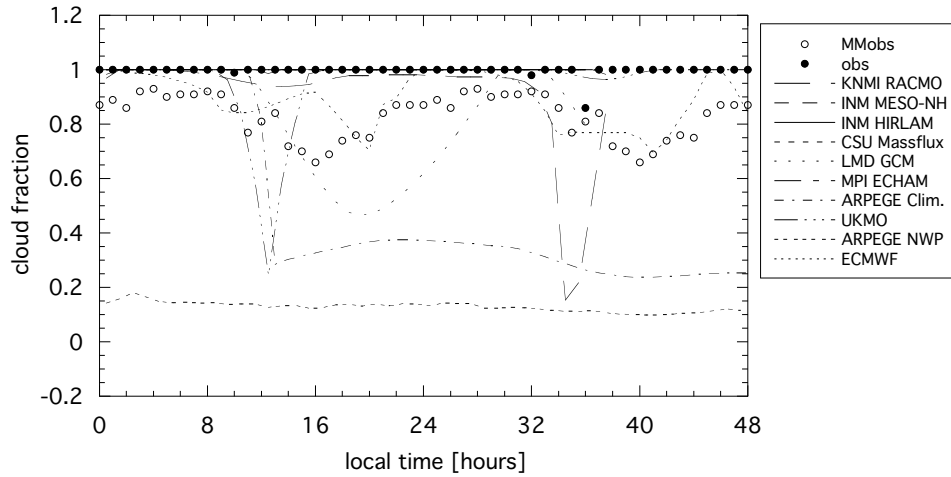


Figure 8: The observed cloud cover (filled dots) and its monthly mean (open circles) and results from Single-Column Model simulations as a function of time for 14 and 15 July 1987 (denoted from 0 to 48 hours Local Time). The linestyles are according to the legend.

Model	Conv_Off	Conv_On	Conv_Off_HR	Conv_On_HR
KNMI RACMO	213.8	2.2	81.8	0.6
MPI ECHAM	256.1	62.9	107.2	113.1
ECMWF	65.7	95.6	-	-
INM HIRLAM	410.9	401.8	-	-

Table 4: The mean LWP [$g\ m^{-2}$] from 1200 to 3600 h LT for four sensitivity experiments. Conv_Off (Conv_On) is performed with the convection scheme switched off (on), and the extension ‘_HR’ denotes a run with a finer vertical resolution. In all the simulations the precipitation scheme was turned off.

Conv_On_HR, respectively.

Table 4 displays the diurnal mean LWP from four SCMs. It appears that for the RACMO model simulations with the convection scheme turned on, cumulus convection is triggered leading to a very rapid entrainment of dry air into the boundary layer and a subsequent rapid decline of the cloud liquid-water path. Suprisingly, in ECMWF the liquid-water path increases when the convection scheme is turned on. This is caused by the detrainment of cloud liquid water by the convection scheme which is an important source of cloud liquid water in the ECMWF cloud scheme (see also Lenderink et al. (2003)). Also, the experiments illustrate the sensitivity of the model results to the vertical resolution used. In the RACMO and ECHAM models, for simulations with the convection scheme turned off, an increase in the vertical resolution leads to a decrease in the mean LWP by about a factor of two. Lastly, the HIRLAM model sensitivity experiments suggest that in the operational version of the model the precipitation scheme is very actively removing liquid water from the cloud (see Table 3), as the mean LWP increases by more than a factor of 4 if the precipitation scheme is switched off.

b. Turbulence structure

The turbulence observations collected by means of a tethered balloon during FIRE I, discussed in detail by Hignett (1991), facilitate a comparison with the results obtained from the LES models. In particular, we will consider the vertical velocity variance ($\overline{w'w'}$) and the buoyancy flux $B = \frac{g}{\theta_0} \overline{w'\theta'_v}$, with g the acceleration due to gravity, and $\theta_0 \approx 300K$ a reference temperature. The observations and the LES results are presented for both night-time and daytime in Figure 9. The LES results are in a good qualitative agreement with the observations and fall within the range of scatter in the observations, although the vertical velocity variance during night-time seems to be slightly overpredicted by most of the LES models. It can be concluded that the LES models are all capable of reproducing the observed turbulence structure during the diurnal cycle fairly well.

Clearly, there are distinct differences in the turbulence structure during daytime and night-time. During the night long-wave radiative cooling near cloud top is the dominant process that drives the turbulent mixing throughout the boundary

layer. In addition, latent heat release effects support a positive buoyancy flux in the cloud layer. The maximum vertical velocity variance is located in the upper half of the boundary layer. During the day the effect of short-wave radiative absorption in the cloud layer becomes manifest. The short-wave radiative warming of the cloud layer leads to a significant reduction of the buoyancy flux. The slightly negative buoyancy fluxes in the middle of the boundary layer tend to damp the vertical turbulent motions leading to a minimum vertical velocity variance near the middle of the boundary layer. This vertical velocity variance profile characterizes a decoupled boundary layer and indicates that the moist turbulent eddies driven from the surface cannot reach the cloud layer anymore. Because entrainment maintains a steady supply of relatively warm and dry air from above the inversion into the cloud layer, the cloud layer tends to thin during daytime, as clearly illustrated from the LWP evolution shown in Figure 4. Because decoupling leads to different heating and moistening rates in the sub-cloud and cloud layer, conserved quantities like θ_l and q_t can not be maintained in a vertically well-mixed state anymore.

The interaction between entrainment rate, buoyancy fluxes and vertical velocity variance is nicely illustrated from the LES results during the night-time period. The IMAU model generates the largest entrainment rate, though it has the lowest vertical velocity variances. This indicates that there is no linear relation between the vertical velocity variance and the entrainment rate. Below the shallow layer that is radiatively cooled the buoyancy flux is determined by the entrainment flux and a fixed radiative flux divergence, where a larger entrainment rate results in a more negative entrainment buoyancy flux. This leads to reduced buoyancy fluxes in the cloud layer and, consequently, smaller vertical velocity variances.

c. Stratocumulus mesoscale fluctuations

The satellite image shown in Figure 1 reveals that the stratocumulus cloud field is dominated by mesoscale structures, a phenomenon that was also frequently observed from aircraft during FIRE I (Moyer and Young, 1994). Cahalan and Snider (1989) analysed observations of the microwave radiometer installed on San Nicholas Island during FIRE I and found that the vertically integrated liquid water content exhibits a $-5/3$ power law up to horizontal length scales well above 100 km. Such mesoscale variations give rise to errors in radiative transfer computations that assume a horizontally homogeneous cloud layer. A horizontally varying liquid water field will decrease the mean albedo compared to a horizontally uniform field, since the albedo of optically thick regions saturates as the optical depth is increased (Cahalan et al., 1994).

Brown (1999) presented results from a series of large-eddy simulations of shallow cumulus convection with different grid resolutions. It appeared that many of the ensemble-averaged turbulence statistics are insensitive to increases in resolution, but the cloud fields change markedly. Because mesoscale fluctuations are frequently dominating stratocumulus cloud structures, an additional large-eddy simulation was performed with an increased horizontal domain size of $25.6 \times 25.6 \text{ km}^2$,

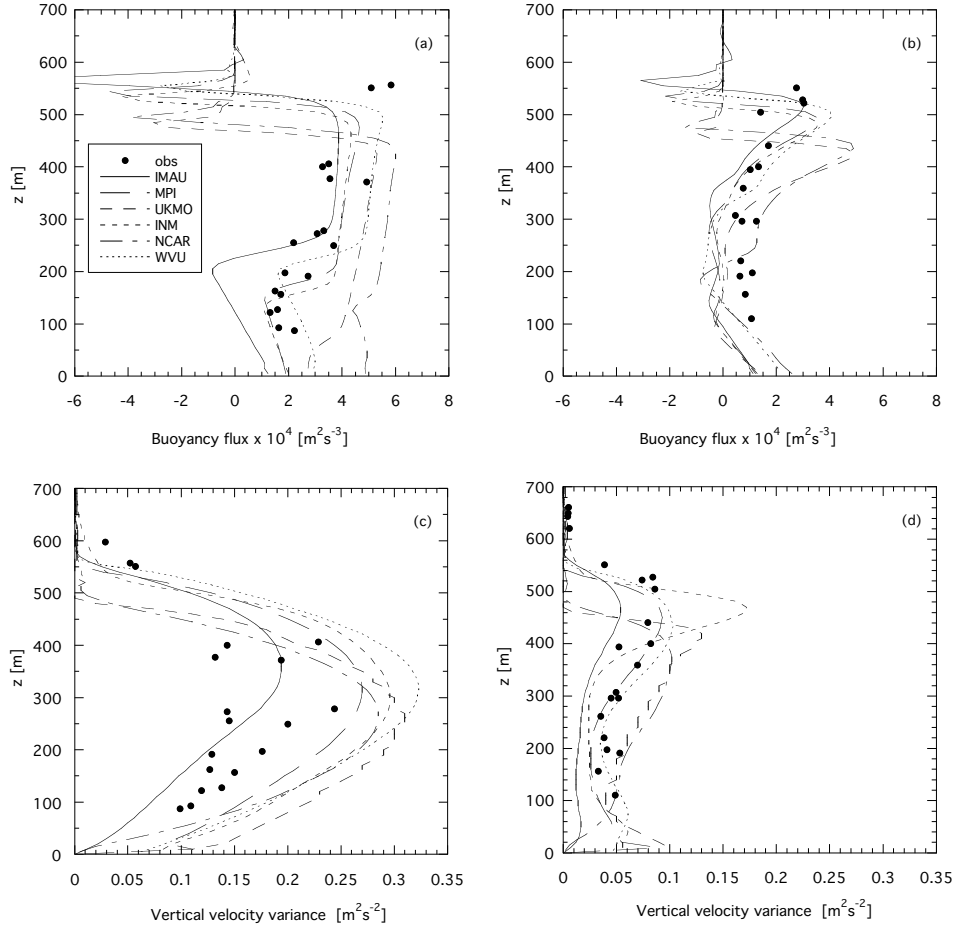


Figure 9: Vertical profiles of observations and LES results. a) Buoyancy flux during a) night-time, b) daytime, and the vertical velocity variance during c) night-time and d) daytime. Note that the LES results represent hourly averaged values between $2300 \leq t < 2400h$ (night-time) and $3500 \leq t < 3600h$ LT (daytime). The linestyles are according to the legend displayed in the upper left panel.

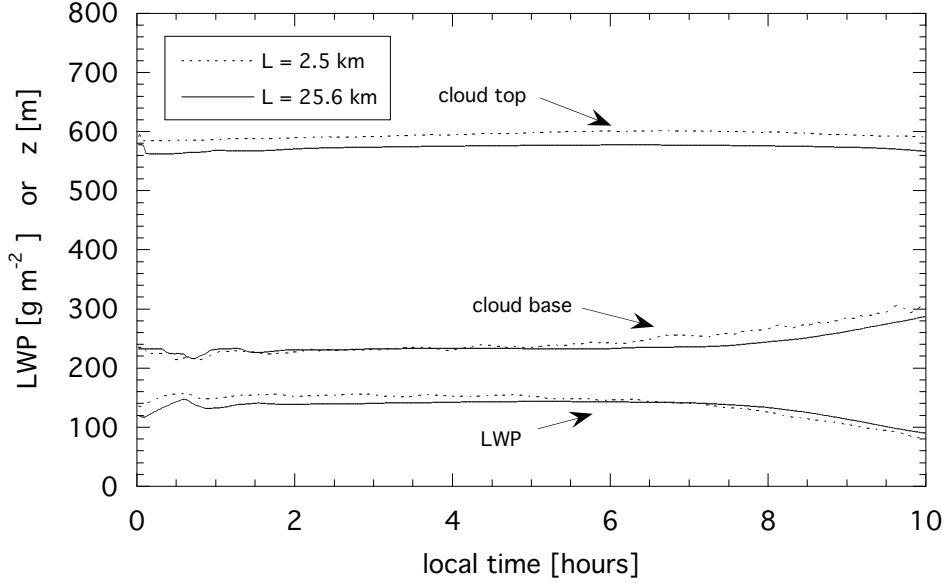


Figure 10: The cloud-base and cloud-top heights, and the liquid-water path as a function of local time. The two different line styles represent results from large-eddy simulations on a small ($L = 2.5 \times 2.5 \text{ km}^2$) and a large horizontal domain ($L = 25.6 \times 25.6 \text{ km}^2$), respectively.

and a resolution of (100, 100, 15) m in the (x, y, z) directions, to allow for the development of mesoscale structures.

Figure 10 shows that the time evolution of the cloud-base and cloud-top heights, and the LWP are hardly sensitive to the horizontal domain sizes. There is a small difference in the cloud-top height at the initialization due to the difference in the vertical grid resolution, 10 and 15 m for the simulation on the small and large horizontal domain, respectively. The fact that the cloud-top and cloud-base heights have the same tendencies indicates that the evolution of the mean state of the boundary layer is consistent in the two simulations.

Figure 11 shows the LWP fields at two different domain sizes after 8 hours of simulation time. Despite the fact that the mean LWPs do not differ very much, the cloud structures appear remarkably different and it appears that the small horizontal domain size acts to limit the growth of mesoscale cloud cells.

For the purpose of radiative transfer computations, the probability density function for the liquid-water path fluctuations, $P(LWP')$, is the relevant quantity to consider (Cahalan et al., 1994). Figure 12 shows $P(LWP')$ for the small and large domain simulations, in addition to $P(q'_t)$, which is relevant for microphysical computations (Wood and Field, 2000). Clearly, the PDFs depend on the horizontal domain size. The simulation at the small domain has relatively more columns that have a LWP close to the mean value, whereas the large domain allows for a broader LWP distribution. A similar distribution is found for the total water content in the

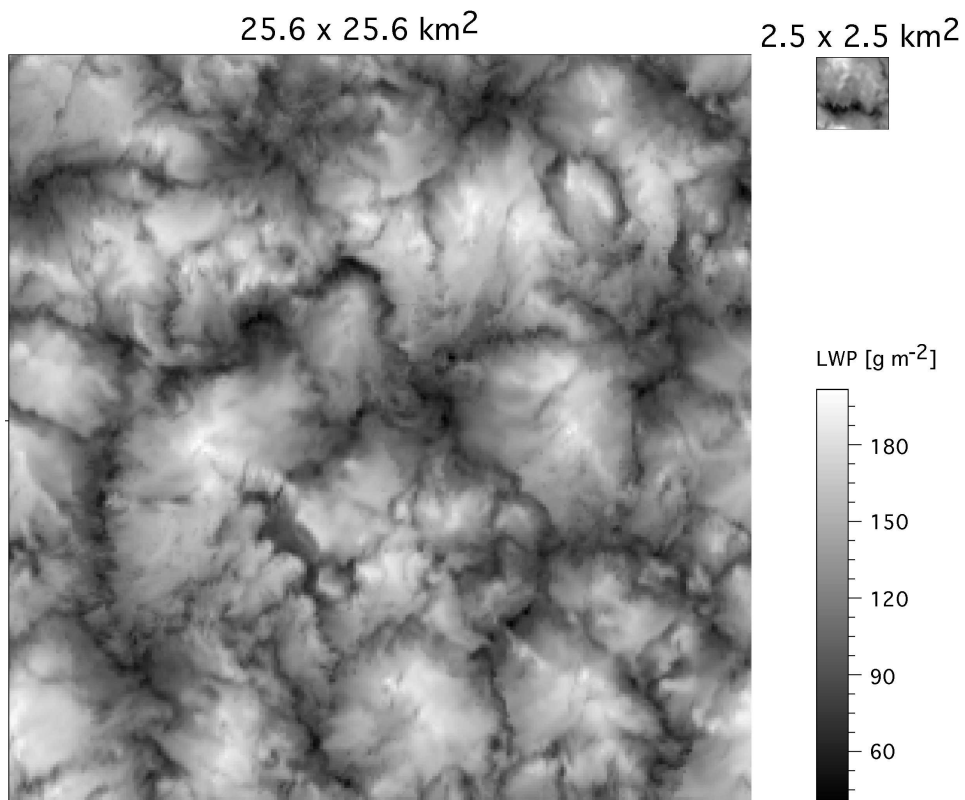


Figure 11: The LWP field at $t = 0800$ h LT from the IMAU LES at the standard domain size ($2.5 \times 2.5 km^2$) and at a large horizontal domain size ($25.6 \times 25.6 km^2$).

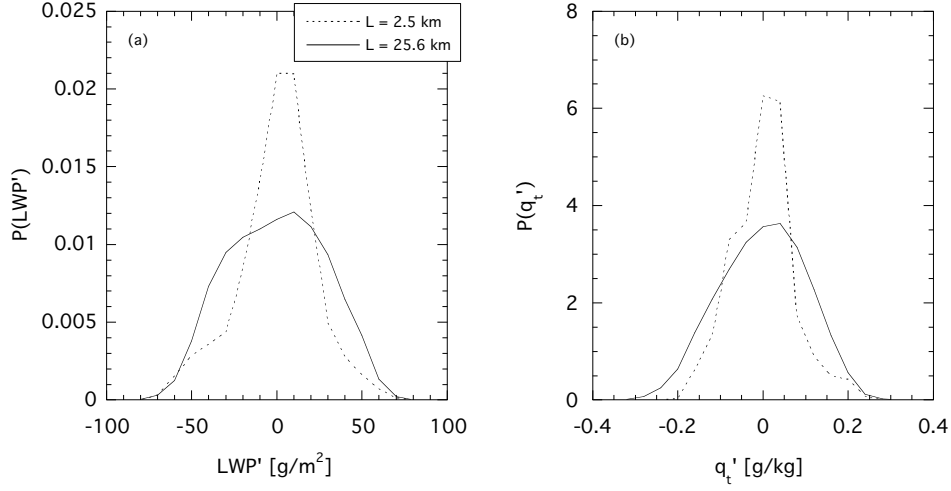


Figure 12: The probability density function P for a) the LWP and b) the total specific humidity fluctuations in the middle of the cloud layer at $t = 0800h$ LT. The two lines represent results from two large-eddy simulations on a small ($L = 2.5 \times 2.5 km^2$) and a large horizontal domain ($L = 25.6 \times 25.6 km^2$), respectively. The line styles are as indicated by the legend.

middle of the cloud layer. De Roode et al. (2004) find that although a small domain size may be sufficient to represent the vertical motions that have a spectral peak at scales on the order of the boundary layer depth, this is not necessarily the case for quantities like the total specific humidity, for which fluctuations tend to grow at much larger scales. If these fluctuations cannot be properly represented by a too small domain, the variance of the quantity will be underestimated. For the PDFs shown in the Figure 12b, the q_t variance is about a factor of two smaller in the small domain simulation, whereas the LWP variance is 812 and 514 $(g m^{-2})^2$ for the large and small domain simulations, respectively.

Los and Duynkerke (2001) investigated the effect of horizontal cloud inhomogeneities on the mean albedo using the Independent Pixel Approximation. They applied a Taylor expansion to conclude that the albedo bias is mainly determined by the variance of the cloud optical depth. This implies that given the same mean value for the LWP, a larger variance for the LWP will effectively lead to a reduction of the mean albedo.

4. Entrainment

The entrainment rates from the LES models shown in Figure 13 were diagnosed by applying the tendency equation (10) for the boundary layer depth z_i . The inversion height z_i is determined from the level where $q_t = 8.1 g kg^{-1}$, obtained by linear interpolation between adjacent grid levels of total water content. Figure 13 shows

		$\frac{\partial \bar{\theta}_l}{\partial t} [K \text{ hr}^{-1}]$		$\frac{\partial \bar{q}_t}{\partial t} [(g \text{ kg}^{-1}) \text{ hr}^{-1}]$
surface flux	$w'\theta_0/z_i$	0.05 ± 0.03	$w'q'_0/z_i$	0.067 ± 0.011
entrainment flux	$w_e \Delta \bar{\theta}_l / z_i$	0.42 ± 0.06	$w_e \Delta \bar{q}_t / z_i$	-0.105 ± 0.015
large-scale advection	$\left(\frac{\partial \bar{\theta}_l}{\partial t}\right)_{LS}$	-0.14	$\left(\frac{\partial \bar{q}_t}{\partial t}\right)_{LS}$	0.055
long-wave radiation	$\Delta F_t / (\rho_0 c_p z_i)$	-0.37		

Table 5: The contribution of the surface fluxes, entrainment, large-scale horizontal advection and radiation to the tendencies of the liquid water potential temperature and the total specific humidity. The mean and standard error for the surface fluxes, the entrainment rate, the inversion height, and the inversion jumps were computed from all the LES results during the night-time period $0100 \leq t < 0400h$ LT.

that there is a clear diurnal cycle in the entrainment rate. Minimum values are found for the daytime period when the buoyancy flux is minimal, and the mean entrainment rate from the six LES results is $w_e = 0.36 \pm 0.03 \text{ cm s}^{-1}$, for $1100 \leq t < 1400h$ LT. During night-time ($0100 \leq t < 0400h$ LT) the mean entrainment rate is larger, $w_e = 0.58 \pm 0.08 \text{ cm s}^{-1}$.

A mixed-layer model was utilized to compute the budgets for heat and moisture during the night (Nicholls, 1984). This model assumes that in the boundary layer the tendency for $\bar{\theta}_l$ does not depend on the height and is given by

$$\frac{\partial \bar{\theta}_l}{\partial t} = \frac{w_e \Delta \bar{\theta}_l + \overline{w'\theta'_{l0}}}{z_i} + \left\langle \frac{\partial \bar{\theta}_l}{\partial t} \right\rangle_{LS} + \langle S_{\theta_l} \rangle, \quad (11)$$

where the operator $\langle \rangle$ gives the vertical mean value for any arbitrary function $f(z)$,

$$\langle f \rangle = \frac{\int_0^{z_i} f(z) dz}{z_i}, \quad (12)$$

and S_{θ_l} is a source term that can represent, for example, the tendency due to a physical process like radiation. The tendency for the total water content is computed similar to (11). If a different heating rate occurs in the sub-cloud layer than in the cloud layer, a situation typically encountered in a decoupled boundary layer during daytime, the mixed layer model cannot be applied. The large-scale forcings like horizontal advection and the long-wave radiative flux divergence were computed in accordance with the case set-up, Eqs. (4) and (5). The LES results were used as input for the turbulent fluxes at the surface and for the entrainment rate at the boundary layer top. From all the LES model results we computed mean values representative for the night-time period, $0100 \leq t < 0400h$ LT. For the turbulent surface fluxes of heat and moisture we obtained $H = 9.5 \pm 6.4 \text{ W m}^{-2}$, $LE = 31.7 \pm 5.1 \text{ W m}^{-2}$.

The results presented in Table 5 indicate that entrainment causes the largest tendencies for both moisture and heat. Note that although the long-wave radiative

Case	Flight	Δq_t [$g\ kg^{-1}$]	$\Delta \theta_l$ [K]	c_b [m]	c_t [m]	w_e [$cm\ s^{-1}$]	w_e (LES) [$cm\ s^{-1}$]
North Sea	511	-3.0	8.4	1000	1320	0.50	
	526	-2.1	7.4	380	830	0.71	
	528	-4.7	8.9	1070	1260	0.24	
	620	-3.0	9.2	960	1300	0.44	
	624	-3.6	9.8	580	1120	0.56	
ASTEX	1	-1.8	4.3	250	740	0.25 ± 0.15	
	2	-1.2	6.2	240	755	1.1 ± 0.5	1.2 ± 0.3
	3	-0.9	5.1	280	770	1.2 ± 1.0	1.9 ± 0.1
	4	-3.0	4.8	610	1070	0.85 ± 0.53	
DYCOMS	1-10	-4.3	$5 \leq \Delta \theta_l \leq 10$	-	$600 \leq c_t \leq 1000$	0.30 ± 0.11	
DYCOMS II	RF01	-7.5	10.0	600	840	0.4 ± 0.1	0.38
FIRE	July 14	-3.0	12.0	233	560	-	0.58 ± 0.08
FIRE	IMAU LES	-3.0	12.0	230	591		0.68
FIRE Exp 1	IMAU LES	-1.0	12.0	160	582		0.77
FIRE Exp 2	IMAU LES	-5.0	12.0	395	598		0.64
FIRE Exp 3	IMAU LES	-3.0	9.0	313	627		1.03

Table 6: Inversion jump properties, cloud-base (c_b) and cloud-top (c_t) heights, and entrainment rates as observed in stratocumulus-topped boundary layers. The observations are described in detail by Nicholls and Leighton (1986) (North Sea), De Roode and Duynkerke (1997) (ASTEX), Kawa and Pearson Jr (1989) (DYCOMS), and Stevens et al. (2003) (DYCOMS II). In DYCOMS the cloud layer was typically 150 to 300 m deep. For FIRE, the jump conditions are from (1), and c_b and c_t represent mean night-time values observed between $0100 \leq t < 0400h$ LT. In addition, entrainment rates from large-eddy simulations are shown. ASTEX Flight 2 was simulated by seven different LES models as part of a GCSS Working Group 1 intercomparison study. The LES of ASTEX Flight 3 by four different models is discussed by Duynkerke et al. (1999). The DYCOMS II case was simulated with the NCAR LES model.

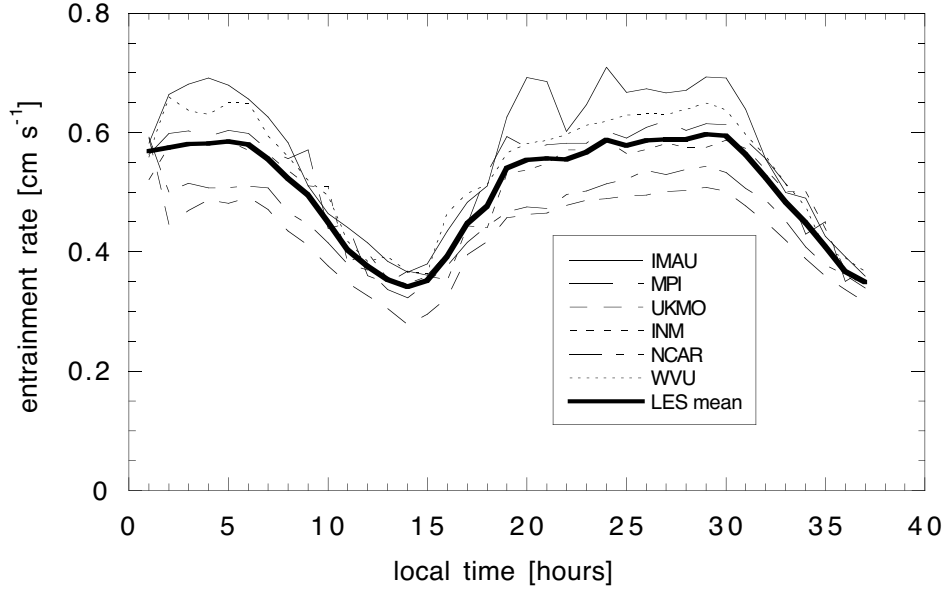


Figure 13: LES results of the entrainment rate as a function of time. In addition, the mean entrainment rate from all LESs is shown. The linestyles are according to the legend.

flux divergence causes a significant cooling, the application of Eq. (5) gives about the same cooling rate for all LES models since the stratocumulus cloud layers are sufficiently optically thick during the entire diurnal cycle. Thus, we conclude that the differences in the entrainment rate among the LES models are the primary source for the variations in the simulated LWP evolution during night-time. During the night, a larger entrainment rate causes smaller LWPs, and vice versa.

A selection of observed entrainment rates is presented in Table 6. Kawa and Pearson Jr (1989) analysed aircraft observations that were collected during daytime in stratocumulus off the Southern California coast as part of the Dynamics and Chemistry of the Marine Stratocumulus (DYCOMS) experiment. They computed entrainment rates in the range of 0.1 to 0.5 cm s^{-1} , with an average value $w_e = 0.30 \pm 0.11 \text{ cm s}^{-1}$. The LES results of the entrainment rate during daytime fall within the range of these observed entrainment rates.

As part of DYCOMS II aircraft observations were collected 500 km west-southwest of San Diego, California. Stevens et al. (2003) used night-time observations collected on 10 July 2001 to compute an average entrainment rate of $w_e = 0.4 \pm 0.1 \text{ cm s}^{-1}$. Figure 3 shows that the rather dry free atmosphere makes the DYCOMS II case unstable with respect to the cloud-top entrainment instability (CTEI) criterion (Randall, 1980; Deardorff, 1980). If a stratocumulus cloud layer is unstable according to this criterion, this may lead to a rapid break-up of the cloud due to enhanced entrainment fluxes of heat and moisture. Obviously, the DYCOMS II observations violate this hypothesis since the cloud layer was found to thicken

during the night. It is also remarkable that the entrainment rate for the DYCOMS II case is smaller than the entrainment rate from LES models for FIRE, contradicting the expectation that the unstable jump conditions will be accompanied by larger entrainment rates.

Chlond and Wolkau (2000) quantified the uncertainty raised from the incomplete knowledge of the environmental parameters that are required to specify the initial and boundary conditions of a particular case study. They explained that in particular uncertainties in the cloud-top jump of total water mixing ratio and the net radiative forcing explain most of the variation of LES solutions. Therefore, additional LESs were performed with the IMAU and MPI models to study the effect of changes in the inversion jumps on the cloud evolution. If the $\Delta\theta_l$ jump is decreased by $3K$ in comparison to the reference case (for more details see FIRE EXP 3 in Table 6, and Figure 3 for the inversion jumps), this results in a significant increase of the entrainment rate. Note that despite the much larger entrainment rate for EXP 3, the cloud layer depth during the first four hours of this simulation is only a fraction smaller than that of the reference case. In contrast, Table 6 shows that modifying the initial moisture jump across the inversion (EXP 1 and 2) has a pronounced effect on the cloud layer depth evolution, although the entrainment rate does not change very much in comparison to the reference case. A more detailed discussion of sensitivity tests performed with the MPI LES model can be found in Chlond et al. (2004).

Entrainment rates on the order of $\sim 1cm\,s^{-1}$ were found from observations collected during the Atlantic Stratocumulus Transition Experiment (ASTEX) (De Roode and Duynkerke, 1997). Flight 3 of the ASTEX First Lagrangian was used for a LES intercomparison study set up by Duynkerke et al. (1999). From four different LES models a mean entrainment rate, $w_e = 1.9 \pm 0.1cm\,s^{-1}$ was found. Note that three of these models are discussed in this paper (IMAU, MPI, INM). So both the observations and LES results indicate larger entrainment rates in comparison to the Pacific stratocumulus cases. This is clearly due to much smaller $\Delta\theta_l$ jumps in the Atlantic stratocumulus cases than those over the Pacific.

5. Suggestions for model improvement

During the EUROCS project various paths have been explored to improve turbulent mixing in the stratocumulus-topped boundary layer, most of them being related to the mixing across the cloud-top. Lock (2004) argues that an explicit parameterization for the entrainment rate results in improved simulations of stratocumulus cloud fields. In a SCM that utilizes an eddy diffusivity approach, the entrainment flux at the top of the cloud layer is computed as,

$$\overline{w'\chi'}|_{z_i} = -K_\chi|_{z_i} \frac{\Delta\chi|_{z_i}}{\Delta z|_{z_i}}, \quad (13)$$

where the operator $\Delta\chi$ gives the vertical difference of χ between two adjacent grid levels. If the cloud layer is capped by a discontinuous inversion with jump

properties $\Delta\bar{\chi}|_{z_i}$, the entrainment flux is, to a good approximation, given by

$$\overline{w'\chi'}|_{z_i} = -w_e\Delta\bar{\chi}|_{z_i}. \quad (14)$$

This equation is exact only if the inversion layer is infinitesimally thin, but since the inversion layers capping stratocumulus have typical depths on the order of a few tens of meters (14) is an appropriate assumption. Eqs. (13) and (14) are equivalent if (Beljaars and Betts, 1992; Lock, 1998; Grenier and Bretherton, 2001)

$$K_\chi|_{z_i} = w_e\Delta z|_{z_i}. \quad (15)$$

This expression provides a consistent means to include an entrainment rate parametrization in a first-order turbulence closure model.

Lenderink and Holtslag (2000) have demonstrated that a coarse vertical resolution can lead to a poor performance of so-called E-I turbulence models. To resolve this problem Chlond et al. (2004) have incorporated a numerical front tracking/capturing method designed by Zhong et al. (1996) which allows the computation of propagating phase boundaries. The advantage of this formulation is that it permits the stratocumulus top to lie between vertical grid levels, continuously evolves with time, and there is no spurious numerical entrainment.

To improve vertical mixing in the (cloud-topped) boundary layer Lenderink and Holtslag (2004) propose a modified length-scale formulation in terms of a vertical integral of the stability. It is aimed to solve problems that arise when the local stability is considered, for example, by a Richardson number, and improves mixing near the surface.

The SCM sensitivity tests with the convection scheme either switched on or off indicate that it may be desirable to develop a single scheme to represent the clear convective boundary layer, stratocumulus and cumulus (De Roode et al., 2000; Lappen and Randall, 2001). Sanchez and Cuxart (2004) discuss a master length scale that is based on Bougeault and Lacarrère (1989) which is also applicable to cumulus-topped boundary layers. Cheinet and Teixeira (2003) suggest that an eddy-diffusivity approach may be applied to cumulus convection as well, whereas Cheinet (2003) tests a multiple mass-flux approach in which clear and cloudy convective plumes are explicitly represented.

The quality of simulations that apply an explicit entrainment rate parameterization such as (15) still depends on the accuracy of the entrainment rate parameterization itself. The scaling behavior of entrainment is still not yet fully understood and remains a major challenge (Turton and Nicholls, 1987; Lewellen and Lewellen, 1998; Lock, 1998; VanZanten et al., 1999; Moeng, 2000; Lilly, 2002). The need for further improvement of entrainment parameterizations was demonstrated by Stevens (2002) who applied mixed-layer theory to synthesize and evaluate several existing entrainment parametrizations for the stratocumulus-topped boundary layer. His results illustrated that these entrainment parametrizations exhibit marked differences. Such differences imply a factor of two differences in climatologically important properties such as the LWP and boundary-layer depth.

Entrainment rate parametrizations usually include a measure of the buoyancy forcing. Because the buoyancy flux in the STBL is generally not a linear function of height, one may consider its vertical integral or the convective velocity scale w_* (Grenier and Bretherton, 2001),

$$w_* = \left(2.5 \frac{g}{\theta_0} \int_0^{z_i} \overline{w'\theta'_v} dz \right)^{1/3}. \quad (16)$$

Scaling the entrainment rate in stratocumulus is complicated not only because the buoyancy flux depends on the entrainment rate, but also since the number of free parameters that determine the vertical profile of the buoyancy flux is much larger than that for the dry convective boundary layer. In the latter case, the entrainment rate is proportional to the ratio of the surface buoyancy flux $\overline{w'\theta'_{v0}}$ and the buoyancy jump across the inversion $\Delta\theta_v$. However, the total water flux gives a large contribution to the buoyancy flux in a stratocumulus cloud layer (Stevens, 2002), which is due to the condensation and evaporation of liquid water droplets. For this reason, the surface moisture flux, the total specific humidity jump across the inversion, the cloud-base and cloud-top heights, and the long-wave radiative flux divergence at the cloud top are all relevant quantities. In summary, if we assume that the entrainment rate depends on the vertical profile of the buoyancy flux, a general scaling expression will depend on the following (conserved) quantities

$$w_e = f(\overline{w'\theta'_v}(z)) = f(\overline{w'\theta'_{v0}}, \overline{w'q'_{v0}}, \Delta\theta_l, \Delta q_t, c_b, c_t, \Delta F_t). \quad (17)$$

In addition, short-wave radiative absorption in the cloud layer during daytime, windshear, and drizzle also affect the buoyancy flux profile. The sensitivity of the buoyancy flux to the quantities summarized above, and the role of the entrainment rate on the buoyancy flux vertical profile can all be clearly illustrated by means of a mixed layer model Nicholls (1984). In this context it is interesting to note that Lewellen and Lewellen (2004) present approximate expressions for the buoyancy flux formulated in terms of the liquid water potential temperature and total water profiles, and their respective flux profiles. The predictions compare favorably with the results of an extensive set of large-eddy simulations, including this EUROCS stratocumulus case.

6. Conclusions

Results of numerical simulations of the EUROCS diurnal cycle of stratocumulus are discussed. In total six Large-Eddy Simulation models and ten Single Column Models participated in this study. The models were initialized on the basis of observations that were collected in stratocumulus off the coast of California during FIRE I, in July 1987. The LES results of the surface energy balance and the turbulence structure of the STBL during the diurnal cycle are compared with observations. The accuracy of the SCMs, which are taken from various General

Circulation Models, is assessed from a comparison of the modeling results with the observed cloud evolution and results from the LESs.

The observed diurnal cycle of stratocumulus is characterized by a cloud layer which gradually thickens during the night, whereas during the day the cloud layer thins due to short-wave radiative absorption and decoupling. The latter state is characterized by slightly negative buoyancy fluxes and a minimum vertical velocity variance near the cloud base. This implies that surface-driven, moist thermals can not penetrate the cloud layer anymore, while entrainment maintains a steady supply of relatively warm and dry air from just above the inversion into the cloud layer. This results in a distinct diurnal cycle of the LWP, which has minimum values during the day. During the night the vertical velocity variance has one single peak near the middle of the boundary layer. The observed turbulence structure, and the LWP temporal evolution are consistently reproduced by all the LES models.

More than half of the participating single-column models predict cloud layers that are too thin, and in particular during the day about half of the models give a cloud cover less than unity. Consequently, in these models the downwelling short-wave radiation reaching the surface is much larger than is observed. Because the cloud-top height computed by the SCMs is found to be systematically lower in comparison to the observations and the LES results, it is likely that the entrainment rates in these SCMs are too low. In a GCM it is therefore vital that the entrainment rate in a STBL is parametrized accurately. Several suggestions for improvements of parameterizations for the cloudy boundary layer based on this EUROCS stratocumulus case can be found in this special issue. Basically, model improvements are basically sought in terms of explicit entrainment parameterizations, a better representation of a sharp inversion in a vertically coarse resolution, modified length scale formulations, and parameterizations that can be applied not only to the clear convective boundary layer and stratocumulus, but also to cumulus.

In order to determine the process that is most important for the boundary-layer temporal evolution, a mixed-layer analysis of the budgets of moisture and heat was performed. It is found that entrainment is the dominant process in modifying the thermodynamic state of the boundary layer during the night. The entrainment rates modeled by the different LES models appear rather consistent, with typical variations in the LES entrainment rates on the order of 1 mm s^{-1} . Such small differences are sufficient to cause significant deviations in the modeled LWP evolution and, consequently, in the net downwelling short-wave radiation during the day.

From a comparison between observations and results from large-eddy simulations of stratocumulus over the Pacific (FIRE I, DYCOMS I, DYCOMS II) and the Atlantic Ocean (ASTEX), we found that the smallest entrainment rates are found for the Pacific cases. Typically, the observed inversion jumps of the liquid water potential temperature were larger for the Pacific stratocumulus cases than for the Atlantic cases. The Pacific cases seem to have a rather persistent character, whereas the ASTEX First Lagrangian observed a transition from stratocumulus to cumulus penetrating thin and broken stratocumulus above. The entrainment rate observed

in a persistent nocturnal STBL during DYCOMS II (Stevens et al., 2003) is found to be smaller than the mean entrainment rate obtained from the LESs of the FIRE I case for the night-time period, despite the fact that the DYCOMS II case has a less stable inversion stratification than the FIRE I case. This DYCOMS II case serves as a new GCSS working group 1 model intercomparison study, and it is aimed that the entrainment rate in a stratocumulus layer which satisfies the cloud-top entrainment instability criterion proposed by Randall (1980) and Deardorff (1980) will be subject to further analysis. In addition, the role of drizzle will be explored.

It is found that from a large-eddy simulation on a large horizontal domain mesoscale fluctuations in the LWP field develop, which is in accord with frequent satellite observations of stratocumulus fields. An analysis of the probability density functions of the LWP and the total specific humidity shows that they are much broader for the larger domain simulation. Because the mesoscale fluctuations tend to grow gradually with time (De Roode et al., 2004), they may not be of importance for simulations of relatively short time scales, $t < 3h$, but for longer, such as diurnal time scales, the spectral broadening in the liquid water field may become relevant. Lastly, to study the effect of horizontal inhomogeneities of the LWP distribution, it is recommended to use a much larger LES horizontal domain than a typical LES domain of, for example, $3 \times 3 km^2$ in the horizontal.

Acknowledgement The investigations were supported by the European Project on Cloud Systems in Climate Models (EUROCS), contract EVK2-CT-1999-00051. M. C. van Zanten acknowledges the support received from NSF grant ATM-0097053 and Foundation for Fundamental Research on Matter (FOM). S. R. de Roode received support from the Netherlands Organization for Scientific Research (NWO). The computations performed by M. C. van Zanten and S. R. de Roode were sponsored by the National Computing Facilities Foundation (NCF) for the use of super-computer facilities. D. Lewellen’s research was supported by the Office of Naval Research (ONR) Grant N00014-98-1-0595.

A Delta-Eddington approximation for short-wave radiation

The net short-wave radiation F_s is obtained from the analytical solution of the delta-Eddington approximation. The delta-Eddington equations are exactly the same as the Eddington equations (Joseph et al., 1976) with transformed asymmetry factor g , single-scattering albedo ω and optical depth τ :

$$\begin{aligned} g' &= \frac{g}{1+g} \\ \omega' &= \frac{(1-g^2)\omega}{1-\omega g^2} \\ \tau' &= (1-\omega g^2)\tau \end{aligned} \tag{18}$$

$z[m]$	$\theta_l[K]$	$q_t[g\ kg^{-1}]$
0	287.50	9.60
595	287.50	9.60
605	299.50	6.60
2095	310.75	2.10
3153	317.29	1.481
5900	326.75	0.379
7600	329.28	0.098
9670	336.61	0.020

Table 7: Liquid water potential temperature and total water content as a function of height for radiation calculations throughout the troposphere.

If we assume ω and g constant with height an analytical solution for the Eddington approximation can be obtained (Shettle and Weinman, 1970):

$$F_s(z) = F_0 \frac{4}{3} [p(C_1 e^{-k\tau(z)} - C_2 e^{k\tau(z)}) - \beta e^{-\frac{\tau(z)}{\mu_0}}] + \mu_0 F_0 e^{-\frac{\tau(z)}{\mu_0}} \quad (19)$$

with:

$$\begin{aligned} k &= [3(1-\omega)(1-\omega g)]^{1/2} \quad , \quad \alpha = 3\omega\mu_0^2 \frac{1+g(1-\omega)}{4(1-k^2\mu_0^2)} \\ p &= \left(\frac{3(1-\omega)}{1-\omega g}\right)^{1/2} \quad , \quad \beta = 3\omega\mu_0 \frac{1+3g(1-\omega)\mu_0^2}{4(1-k^2\mu_0^2)}, \end{aligned} \quad (20)$$

and $F_0 = 1100\ \text{Wm}^{-2}$ the downward solar radiation at cloud top. According to microphysical observations during FIRE I discussed by Duda et al. (1991) we prescribe the effective radius, $r_e = 10\ \mu\text{m}$. The values of the constants C_1 and C_2 in (19) are determined from the boundary condition at the surface (albedo $A = 0.05$) and above the cloud. See for further details Shettle and Weinman (1970). From the observed liquid water path on San Nicolas island we have calculated the optical depth from equation (7) with $r_e = 10\ \mu\text{m}$. In Figure 14 we have plotted the measured downward short radiative flux as a function of the calculated optical depth for observations around local noon. Moreover, we have shown the model results for $\mu_0 = \cos \theta_0 = 0.95$, which give somewhat higher values than the observations. This may possibly be explained by the fact that the observed clouds are horizontally inhomogeneous as opposed to what is assumed in the delta-Eddington method, or a systematic bias in the observed cloud optical depth.

LES and SCM models that do not use the suggested radiation codes may need a temperature and humidity profile above 1200 m for the radiation calculations. Table 7 gives some typical numbers that were derived from radiosonde stations along the Californian coast. If values at intermediate levels are needed they can be obtained through linear interpolation.

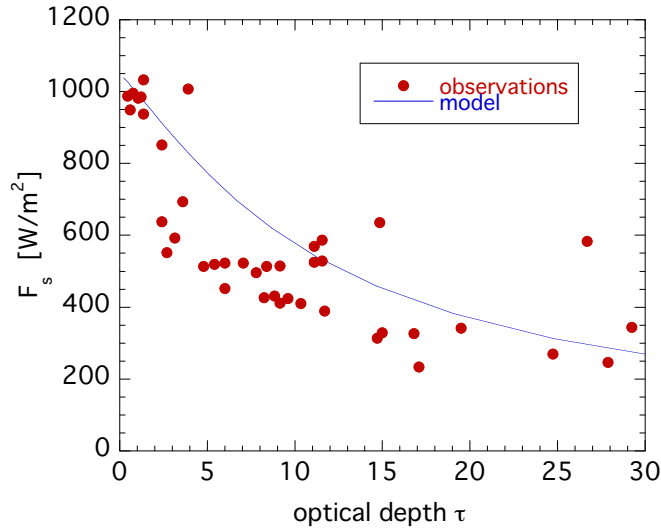


Figure 14: The downward short-wave irradiance around solar noon ($\mu_0 = 0.95$) at the surface as a function of optical depth: observations on San Nicolas island (dots) and model calculations (line).

References

- Albrecht, B. A., C. W. Fairall, D. W. Thomson, A. B. White, J. B. Snider, and W. H. Schubert, 1990: Surface-based remote sensing of the observed and the adiabatic liquid water content of stratocumulus clouds. *gri*, **17**, 89–92.
- Albrecht, B. A., D. A. Randall, and S. Nicholls, 1988: Observations of marine stratocumulus clouds during FIRE. *Bull. Am. Meteorol. Soc.*, **69**, 618–626.
- Beljaars, A. C. M. and A. K. Betts, 1992: Validation of the boundary layer representation in the ECMWF model. *Validation of models over Europe*, ECMWF, Reading, UK.
- Betts, A. K., 1990: The diurnal variation of California coastal stratocumulus for two days of boundary layer soundings. *Tellus*, **42A**, 302–304.
- Blaskovic, M., R. Davies, and J. B. Snider, 1991: Diurnal variation of marine stratocumulus over San Nicolas Island during July 1987. *Mon. Weather Rev.*, **119**, 1469–1478.
- Bougeault, P. and P. Lacarrère, 1989: Parameterization of orography-induced turbulence in a mesobeta-scale model. *Mon. Weather Rev.*, **117**, 1872–1890.
- Bretherton, C. S., S. K. Krueger, M. C. Wyant, P. Bechtold, E. V. Meijgaard, B. Stevens, and J. Teixeira, 1999: A GCSS boundary-layer cloud model inter-comparison study of the first ASTEX Lagrangian experiment. *Boundary-Layer Meteorol.*, **93**, 341–380.

- Bretherton, C. S., T. Uttal, C. W. Fairall, S. Yuter, R. Weller, D. Baumgardner, K. Comstock, R. Wood, and G. Raga, 2004: The EPIC 2001 stratocumulus study. *Bull. Amer. Meteor. Soc.*, *in press*.
- Brown, A. R., 1999: The sensitivity of large-eddy simulations of shallow cumulus convection to resolution and subgrid model. *Q. J. R. Meteorol. Soc.*, **125**, 469–482.
- Brown, A. R., R. T. Cederwall, A. Chlond, P. G. Duynkerke, J.-C. Golaz, M. Khairoutdinov, D. C. Lewellen, A. P. Lock, M. K. Macvean, C.-H. Moeng, R. A. J. Neggers, A. P. Siebesma, and B. Stevens, 2002: Large-eddy simulation of the diurnal cycle of shallow cumulus convection over land. *Q. J. R. Meteorol. Soc.*, **128**, 1075–1093.
- Cahalan, R. F., W. Ridgway, W. J. Wiscombe, S. Gollmer, and Harshvardhan, 1994: Independent pixel and Monte-Carlo estimates of stratocumulus albedo. *J. Atmos. Sci.*, **51**, 3776–3790.
- Cahalan, R. F. and J. B. Snider, 1989: Marine stratocumulus structure. *Remote Sensing Environ.*, **28**, 95–107.
- Cheinet, S., 2002: *The parameterization of clear and cloudy convective boundary layers*. Ph.D. thesis, Ecole Polytechnique, Paris, 142 pp (Available from Ecole Polytechnique, Paris, France).
- 2003: A multiple mass-flux parameterization for the surface generated convection. part i: Dry plumes. *J. Atmos. Sci.*, **60**, 2313–2327.
- Cheinet, S. and J. Teixeira, 2003: A simple formulation for the eddy-diffusivity parameterization of cloud-topped boundary layers. *Geophys. Res. Lett.*, **30**.
- Chlond, A., F. Müller, and I. Sednev, 2004: Numerical simulation of the diurnal cycle of marine stratocumulus during fire - an eurocs les and scm modeling study. *Q. J. R. Meteorol. Soc.*, submitted for the EUROCS special issue.
- Chlond, A. and A. Wolkau, 2000: Large-eddy simulation of a nocturnal stratocumulus-topped marine atmospheric boundary layer: An uncertainty analysis. *Boundary-Layer Meteorol.*, **95**, 31–55.
- De Roode, S. R. and P. G. Duynkerke, 1997: Observed Lagrangian transition of stratocumulus into cumulus during ASTEX: Mean state and turbulence structure. *J. Atmos. Sci.*, **54**, 2157–2173.
- De Roode, S. R., P. G. Duynkerke, and H. J. J. Jonker, 2004: Large eddy simulation: How large is large enough? *J. Atmos. Sci.*, **61**, 403–421.
- De Roode, S. R., P. G. Duynkerke, and A. P. Siebesma, 2000: Analogies between mass-flux and reynolds-averaged equations. *J. Atmos. Sci.*, **57**, 1585–1598.

- Deardorff, J. W., 1980: Cloud-top entrainment instability. *J. Atmos. Sci.*, **37**, 131–147.
- Duda, D. P., G. L. Stephens, and S. K. Cox, 1991: Microphysical and radiative properties of marine stratocumulus from tethered balloon measurements. *J. Appl. Meteorol.*, **30**, 170–186.
- Duynkerke, P. G. and P. Hignett, 1993: Simulation of diurnal variation in a stratocumulus-capped marine boundary layer during FIRE. *Mon. Weather Rev.*, **121**, 3291–3300.
- Duynkerke, P. G., P. J. Jonker, A. Chlond, M. C. Van Zanten, J. Cuxart, P. Clark, E. Sanchez, G. M. Martin, G. Lenderink, and J. Teixeira, 1999: Intercomparison of three- and one-dimensional model simulations and aircraft observations of stratocumulus. *Boundary-Layer Meteorol.*, **92**, 453–487.
- Duynkerke, P. G. and J. Teixeira, 2001: Comparison of the ECMWF reanalysis with FIRE I observations: Diurnal variation of marine stratocumulus. *J. Climate*, **14**, 1466–1478.
- Grenier, H. and C. S. Bretherton, 2001: A moist PBL parameterization for large-scale models and its application to subtropical cloud-topped marine boundary layers. *Mon. Weather Rev.*, **129**, 357–377.
- Guichard, F., J. Petch, and Co-authors, 2004: Modelling of the diurnal cycle of deep convection over land. *Q. J. R. Meteorol. Soc.*, submitted for the EUROCS special issue.
- Hignett, P., 1991: Observations of the diurnal variation in a cloud-capped marine boundary layer. *J. Atmos. Sci.*, **48**, 1474–1482.
- Hogg, D. C., F. O. Guiraud, J. B. Snider, M. T. Decker, and E. R. Westwater, 1983: A steerable dual-channel microwave radiometer for measurements of water vapor and liquid in the troposphere. *J. Clim. Appl. Meteorol.*, **22**, 789–806.
- Jakob, C., 1999: Clouds in the ECMWF Re-Analysis. *J. Climate*, **12**, 947–959.
- Joseph, J. H., W. J. Wiscombe, and J. A. Weinman, 1976: The delta-Eddington approximation for radiative flux transfer. *J. Atmos. Sci.*, **33**, 2452–2459.
- Kawa, S. R. and R. Pearson Jr, 1989: An observational study of stratocumulus entrainment and thermodynamics. *J. Atmos. Sci.*, **46**, 2650–2661.
- Klein, S. A. and D. L. Hartmann, 1993: The seasonal cycle of low stratiform clouds. *J. Climate*, 1587–1606.
- Kuo, H. and W. H. Schubert, 1988: Stability of cloud-topped boundary layers. *Q. J. R. Meteorol. Soc.*, **114**, 887–917.

- Lappen, C. L. and D. A. Randall, 2001: Toward a unified parameterization of the boundary layer and moist convection. Part I: A new type of mass-flux model. *J. Atmos. Sci.*, **58**, 2021–2036.
- Lenderink, G. and A. A. M. Holtslag, 2000: Evaluation of the kinetic energy approach for modelling turbulent fluxes in stratocumulus. *Mon. Weather Rev.*, **128**, 244–258.
- 2004: An updated length scale formulation for turbulent mixing in clear and cloudy boundary layers. *Q. J. R. Meteorol. Soc.*, submitted for the EUROCS special issue.
- Lenderink, G., A. P. Siebesma, S. Cheinet, S. Irons, C. G. Jones, P. Marquet, F. Müller, D. Olmeda, J. Calvo, E. Sanchez, and P. M. M. Soares, 2003: The diurnal cycle of shallow cumulus clouds over land: A single column model intercomparison study. *Q. J. R. Meteorol. Soc.*, submitted for the EUROCS special issue.
- Lewellen, D. C. and W. S. Lewellen, 1998: Large eddy boundary layer entrainment. *J. Atmos. Sci.*, **55**, 2645–2665.
- 2004: buoyancy flux modeling for cloudy boundary layers. *J. Atmos. Sci.*, in press.
- Lilly, D., 2002: Entrainment into cloud-topped mixed layers: A new closure. *J. Atmos. Sci.*, **59**, 3353–3361.
- Lock, A. P., 1998: The parameterization of entrainment in cloudy boundary layers. *Q. J. R. Meteorol. Soc.*, **124**, 2729–2753.
- 2004: The sensitivity of a GCM’s marine stratocumulus to cloud-top entrainment. *Q. J. R. Meteorol. Soc.*, submitted for the EUROCS special issue.
- Los, A. and P. G. Duynkerke, 2001: Parametrization of solar radiation in inhomogeneous stratocumulus: Albedo bias. *Q. J. R. Meteorol. Soc.*, **127**, 1593–1614.
- Ma, C.-C., C. R. Mechoso, A. W. Robertson, and A. Arakawa, 1996: Peruvian stratus clouds and the tropical Pacific circulation: A coupled ocean-atmosphere GCM study. *J. Climate*, **9**, 1635–1645.
- Miller, R. L., 1997: Tropical thermostats and low cloud cover. *J. Climate*, **10**, 409–440.
- Moeng, C. H., 2000: Entrainment rate, cloud fraction and liquid water path of PBL stratocumulus clouds. *J. Atmos. Sci.*, **57**, 3627–3643.
- Moeng, C. H., W. R. Cotton, C. S. Bretherton, A. Chlond, M. Khairoutdinov, S. Krueger, W. S. Lewellen, M. K. MacVean, J. R. M. Pasquier, H. A. Rand, A. P.

- Siebesma, B. Stevens, and R. I. Sykes, 1996: Simulation of a stratocumulus-topped planetary boundary layer: Intercomparison among different numerical codes. *Bull. Am. Meteorol. Soc.*, **77**, 261–278.
- Moyer, K. A. and G. S. Young, 1994: Observations of mesoscale cellular convection from the marine stratocumulus phase of FIRE. *Boundary-Layer Meteorol.*, **71**, 109–133.
- Neiburger, M., 1960: The relation of air mass structure to the field of motion over the eastern North Pacific Ocean in summer. *Tellus*, **12**, 31–40.
- Nicholls, S., 1984: The dynamics of stratocumulus: Aircraft observations and comparisons with a mixed layer model. *Q. J. R. Meteorol. Soc.*, **110**, 783–820.
- Nicholls, S. and J. Leighton, 1986: An observational study of the structure of stratiform cloud sheets: Part I. Structure. *Q. J. R. Meteorol. Soc.*, **112**, 431–460.
- Nigam, S., 1997: The annual warm to cold phase transition in the eastern equatorial pacific: Diagnosis of the role of stratus cloud-top cooling. *J. Climate*, **10**, 2447–2467.
- Norris, J. R., 1997a: Low cloud type over the ocean from surface observations. Part I: Relationship to surface meteorology and the vertical distribution of temperature and moisture. *J. Climate*, **11**, 369–382.
- 1997b: Low cloud type over the ocean from surface observations. Part II: Geographical and seasonal variations. *J. Climate*, **11**, 383–403.
- Philander, S. G. H., D. Gu, D. Halpern, G. Lambert, N.-C. Lau, T. Li, and R. C. Pacanowski, 1996: Why the ITCZ is mostly north of the equator. *J. Climate*, **9**, 2958–2972.
- Randall, D. A., 1980: Conditional instability of the first kind upside down. *J. Atmos. Sci.*, **37**, 125–130.
- Sanchez, E. and J. Cuxart, 2004: A buoyancy based mixing length proposal for cloudy boundary layers. *Q. J. R. Meteorol. Soc.*, submitted for the EUROCS special issue.
- Schubert, W. H., S. K. Cox, P. E. Ciesielski, and C. M. Johnson-Pasqua, 1987: Operation of a ceilometer during the FIRE marine stratocumulus project. Atmospheric Science Paper No. 420. Technical report, Colorado State University, Ft. Collins, CO 80523, USA, 34pp.
- Shettle, E. P. and J. A. Weinman, 1970: The transfer of solar irradiance through inhomogeneous turbid atmospheres evaluated by Eddingtons approximation. *J. Atmos. Sci.*, **27**, 1048–1055.

- Siebesma, A. P., C. S. Bretherton, A. Brown, A. Chlond, J. Cuxart, P. G. Duynkerke, H. Jiang, M. Khairoutdinov, D. Lewellen, C.-H. Moeng, E. Sanchez, B. Stevens, and D. E. Stevens, 2003: A large eddy simulation intercomparison study of shallow cumulus convection. *J. Atmos. Sci.*, **60**, 1201–1219.
- Siebesma, A. P., C. Jakob, and Co-authors, 2004: Cloud representation in general circulation models over the northern pacific ocean: A EUROCS intercomparison study. *Q. J. R. Meteorol. Soc.*, submitted for the EUROCS special issue.
- Stevens, B., 2002: Entrainment in stratocumulus-topped mixed layers. *Q. J. R. Meteorol. Soc.*, **128**, 2663–2690.
- Stevens, B., A. S. Ackerman, B. A. Albrecht, A. R. Brown, A. Chlond, J. Cuxart, P. G. Duynkerke, D. C. Lewellen, M. K. MacVean, R. A. J. Neggers, E. Sanchez, A. P. Siebesma, and D. E. Stevens, 2001: Simulations of trade wind cumuli under a strong inversion. *J. Atmos. Sci.*, **58**, 1870–1891.
- Stevens, B., D. H. Lenschow, I. Faloona, C.-H. Moeng, D. K. Lilly, B. Blomquist, G. Vali, A. Bandy, T. Campos, H. Gerber, S. Haimov, B. Morley, and D. Thorton, 2003: On entrainment rates in nocturnal marine stratocumulus. *Submitted for publication in the Q. J. Roy. Met. Soc.*.
- Turton, J. D. and S. Nicholls, 1987: A study of the diurnal variation of stratocumulus using a multiple mixed layer model. *Q. J. R. Meteorol. Soc.*, **113**, 969–1009.
- VanZanten, M. C., P. G. Duynkerke, and J. W. M. Cuijpers, 1999: Entrainment parameterization in convective boundary layers. *J. Atmos. Sci.*, **56**, 813–828.
- White, A. B., 1999: *Temperature and humidity structure parameters deduced from sodar and radar reflectivities: An analysis of data from the marine stratocumulus phase of FIRE*. Master’s thesis, Pennsylvania State University, Available from Pennsylvania State University, Department of Meteorology, University Park, PA 16802, USA, 137 pp.
- Wood, R., C. S. Bretherton, and D. L. Hartmann, 2002: Diurnal cycle of liquid water path over the subtropical and tropical oceans. *Geophys. Res. Lett.*, **29**, Art. No. 2092.
- Wood, R. and P. R. Field, 2000: Relationships between total water, condensed water, and cloud fraction in stratiform clouds examined using aircraft data. *J. Atmos. Sci.*, **57**, 1888–1905.
- Yu, J.-Y. and C. R. Mechoso, 1999: Links between annual variations of Peruvian stratocumulus clouds and of SST in the eastern equatorial Pacific. *J. Climate*, **12**, 3305–3318.
- Zhong, X., T. Y. Hou, and P. G. LeFloch, 1996: Computational methods for propagating phase boundaries. *J. Comp. Phys.*, **124**, 192–216.